

Iterative multiscale finite-volume method

Hadi Hajibeygi^{a,*}, Giuseppe Bonfigli^a, Marc Andre Hesse^b, Patrick Jenny^a

^a Institute of Fluid Dynamics, Sonneggstrasse 3, ETH Zurich, Zurich CH-8092, Switzerland

^b Department of Energy Resource Engineering, Stanford University, Stanford, CA 94305-2220, USA

ARTICLE INFO

Article history:

Received 7 March 2008

Received in revised form 11 June 2008

Accepted 12 June 2008

Available online 26 June 2008

Keywords:

Iterative multiscale methods
Multiscale finite-volume method
Elliptic problem
Poisson equation
Line relaxation
Multiphase flow
Porous media

ABSTRACT

The multiscale finite-volume (MSFV) method for the solution of elliptic problems is extended to an efficient iterative algorithm that converges to the fine-scale numerical solution. The localization errors in the MSFV method are systematically reduced by updating the local boundary conditions with global information. This iterative multiscale finite-volume (i-MSFV) method allows the conservative reconstruction of the velocity field after any iteration, and the MSFV method is recovered, if the velocity field is reconstructed after the first iteration. Both the i-MSFV and the MSFV methods lead to substantial computational savings, where an approximate but locally conservative solution of an elliptic problem is required. In contrast to the MSFV method, the i-MSFV method allows a systematic reduction of the error in the multiscale approximation. Line relaxation in each direction is used as an efficient smoother at each iteration. This smoother is essential to obtain convergence in complex, highly anisotropic, heterogeneous domains. Numerical convergence of the method is verified for different test cases ranging from a standard Poisson equation to highly heterogeneous, anisotropic elliptic problems. Finally, to demonstrate the efficiency of the method for multiphase transport in porous media, it is shown that it is sufficient to apply the iterative smoothing procedure for the improvement of the localization assumptions only infrequently, i.e. not every time step. This result is crucial, since it shows that the overall efficiency of the i-MSFV algorithm is comparable with the original MSFV method. At the same time, the solutions are significantly improved, especially for very challenging cases.

© 2008 Elsevier Inc. All rights reserved.

1. Introduction

Natural porous media are typically governed by highly heterogeneous coefficients with complex spatial distributions. While current advances in characterization and data integration provide increasingly detailed descriptions of the subsurface, classical simulation techniques lack the capability to honor all these fine-scale structures. To deal with this resolution gap, various multiscale methods have been developed during the past decade. The aim of these methods is to reduce the computational complexity by incorporating the fine-scale variation of the coefficients into the coarse-scale operator; similar to upscaling methods [1–3]. Upscaling methods aim at coarse-scale descriptions based on effective, tensorial coefficients [4]. In addition, multiscale methods allow to reconstruct a fine-scale velocity field from a coarse-scale pressure solution [5]. This velocity field can be used, for example, to solve the saturation transport equations on the fine grid. Current multiscale methods for flow in heterogeneous porous media can be categorized into multiscale finite-element (MSFE) methods [6], mixed multiscale finite-element (MMSFE) methods [7–9], and multiscale finite-volume (MSFV) methods [10,11], where

* Corresponding author. Tel.: +41 44 632 6034; fax: +41 44 632 1147.

E-mail addresses: hajibeygi@ifd.mavt.ethz.ch (H. Hajibeygi), bonfigli@ifd.mavt.ethz.ch (G. Bonfigli), mhesse@stanford.edu (M.A. Hesse), jenny@ifd.mavt.ethz.ch (P. Jenny).

only the MMSFE and MSFV methods provide conservative fine-scale velocity fields. For problems arising from flow and transport in porous media, a conservative velocity is required for the transport calculations. All these multiscale methods can be applied to compute approximate solutions at reduced computational cost. While the multiscale solutions differ from the reference solutions computed with the same standard numerical scheme on the fine grid, convergence with respect to coarse-grid refinement was proved for permeability fields characterized by two separable scales [7,11,12]. On the other hand, it was shown that MSFE methods do not converge for problems without scale separation [11–14].

The accuracy of multiscale solutions was demonstrated for a wide range of test cases [15,16], but so far no a priori error estimation was possible. Of particular interest are predictions of the error introduced by the multiscale localization assumptions as a function of coarse-grid resolution, aspect ratio, and permeability field.

The multiscale methods considered here are based on local numerical solutions of the fine-scale problem (honoring the provided permeability field). From these local fine-scale solutions one can derive transmissibilities for the coarse problem. The quality of multiscale results depends on the localization conditions employed to solve the local fine-scale problems. Typically, errors introduced by a multiscale method are most prominent in the presence of large (with respect to the coarse cells) coherent structures with high permeability contrasts. Typical examples are extended, nearly impermeable shale layers [17]. In that case, there exists no general accurate localization assumption. For further improvements, global information can be employed to enhance the boundary conditions of the local problems. Existing methods of this kind rely on an initial global fine-scale solution [8,9,15,18]. However, for problems with high phase viscosity ratios, frequently changing boundary conditions or varying well rates, the value of such an approach is questionable.

Another possibility is to improve the coarse operator iteratively. The adaptive local-global (ALG) upscaling approach is based on global iterations to obtain a self-consistent coarse-grid description [19,20]. It was shown that ALG leads to more accurate solutions than local upscaling methods. Recently, ALG was employed to improve the local boundary conditions in the multiscale finite volume element method (ALG-MSFVE) [21]. Chen et al. [19] showed that ALG leads to asymptotic solutions for large numbers of iterations, but typically these solutions are different from standard fine-scale solutions and the error due to ALG is problem dependent.

In this paper we present an iterative multiscale finite-volume (i-MSFV) method. The i-MSFV solutions converge to the corresponding fine-scale reference results, which is achieved by iterative improvement of the boundary conditions of the local problems. In previous iterative multiscale methods, such as the ALG-MSFVE method, the coarse multiscale operator is iteratively improved by updating all basis functions. This is computationally expensive and avoided here by using correction functions. In each iteration only the correction functions are updated, while the basis functions and hence the coarse operator remain unchanged. While the i-MSFV method can still be employed as a typical multiscale method (without iterations it is identical to the MSFV method) it can also be used as an efficient linear solver. Moreover, since it is possible to construct a conservative fine-scale velocity field at each iteration level, the i-MSFV method can be operated anywhere between these two extremes. With the i-MSFV method it is possible to control the localization assumptions and therefore, similar to the ALG-MSFVE method, the error can be reduced dramatically by only a few iterations.

This paper is organized as follows. In Section 2 we explain the MSFV method for a general elliptic problem. Based on that, in Section 3 we introduce our i-MSFV method. Then, in Section 4 the convergence behavior of this iterative solver is examined numerically for a wide range of test cases; followed by Section 5, where a spectral analysis of the iteration matrix is presented. In Section 6 we focus on applications to single and multiphase flow in porous media, and finally we conclude the paper in Section 7.

2. The MSFV method

To explain the MSFV method, we consider the elliptic problem

$$-\nabla \cdot (\lambda \cdot \nabla p) = q \quad (1)$$

on the domain Ω with the boundary conditions $\nabla p \cdot \mathbf{n} = f$ and $p(\mathbf{x}) = g$ at $\partial\Omega_1$ and $\partial\Omega_2$, respectively. Note that $\partial\Omega = \partial\Omega_1 \cup \partial\Omega_2$ is the whole boundary of the domain Ω and \mathbf{n} is the outward unit normal vector. The mobility tensor λ is positive definite and the right-hand sides q , f , and g are specified fields.

The MSFV method is designed to efficiently compute approximate solutions of problem (1) for highly heterogeneous coefficients λ and right-hand sides q , e.g. for mobility fields, which depict a high variance, complex correlation structures and which are governed by a large range of length scales.

The MSFV method relies on an imposed coarse grid (solid lines in Fig. 1) and on a dual coarse grid (dashed lines in Fig. 1). The former is composed of M control volumes $\bar{\Omega}_k$ ($k \in [1, M]$) and the latter of N cells $\bar{\Omega}^h$ ($h \in [1, N]$). As illustrated in Fig. 1, each control volume $\bar{\Omega}_k$ contains exactly one node \mathbf{x}_k of the dual coarse grid in its interior. Note that these two grids can be much coarser than the underlying fine grid on which the mobility field is represented. It is also emphasized that the concept is not limited to the simple grids shown in Fig. 1. In principal, very irregular grids or decompositions can be employed. The reduction of degrees of freedom to describe the fine pressure p_f (pressure field on the fine grid) is achieved through the approximation

$$p_f(\mathbf{x}) \approx p'(\mathbf{x}) = \sum_{h=1}^N \left[\sum_{k=1}^M \Phi_k^h(\mathbf{x}) \bar{p}_k + \Phi^h(\mathbf{x}) \right], \quad (2)$$

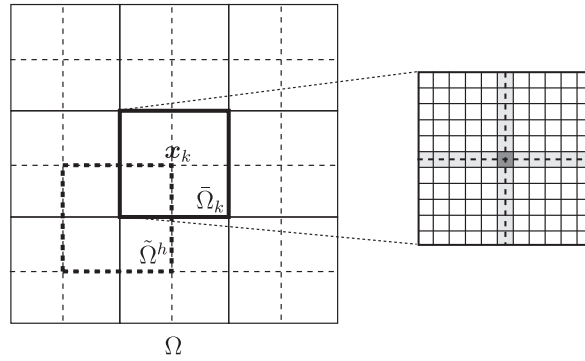


Fig. 1. The computational domain Ω with the coarse grid (solid lines) and the dual coarse grid (dashed lines); solid and dashed bold lines indicate a selected coarse cell $\bar{\Omega}_k$ and a selected dual coarse cell $\tilde{\Omega}_k^h$, respectively. Shown on the right side is an enlarged coarse cell, which contains 11×11 fine cells. The fine-scale boundary volumes of the dual coarse cells, which overlap with their neighbors, are depicted in grey.

where \bar{p}_k are the pressure values at the nodes \mathbf{x}_k . We refer to Φ_k^h as the basis functions and to Φ^h as the correction function. Opposed to classical finite-element methods, basis functions and correction functions are not analytical functions, but local numerical solutions of problem (1) on $\tilde{\Omega}^h$ without and with right-hand side, respectively. Localization can be achieved by employing reduced problem boundary conditions at $\partial\tilde{\Omega}^h$, which is equivalent to

$$(\tilde{\mathbf{n}}^h \cdot \nabla)((\lambda \cdot \nabla \Phi_k^h) \cdot \tilde{\mathbf{n}}^h) = 0 \quad (3)$$

and

$$(\tilde{\mathbf{n}}^h \cdot \nabla)((\lambda \cdot \nabla \Phi^h) \cdot \tilde{\mathbf{n}}^h) = r^h \quad (4)$$

at $\partial\tilde{\Omega}^h$ with $\tilde{\mathbf{n}}^h$ being the unit normal vector pointing out of $\tilde{\Omega}^h$. At the dual-grid nodes \mathbf{x}_l which belong to $\tilde{\Omega}^h$, $\Phi_k^h(\mathbf{x}_l) = \delta_{kl}$ and $\Phi^h(\mathbf{x}_l) = 0$. By construction, outside $\tilde{\Omega}^h$ the Φ_k^h and Φ^h are set to zero. An illustration of 2D basis and correction functions is shown in Fig. 2.

To derive a linear system for the coarse pressure values \bar{p}_k , we substitute expression (2) for p' into Eq. (1) and integrate over $\bar{\Omega}_l$, which leads to

$$-\int_{\bar{\Omega}_l} \nabla \cdot (\lambda \cdot \nabla p') d\Omega = -\int_{\bar{\Omega}_l} \nabla \cdot \left(\lambda \cdot \nabla \left(\sum_{h=1}^N \left(\sum_{k=1}^M \Phi_k^h \bar{p}_k + \Phi^h \right) \right) \right) d\Omega = \int_{\bar{\Omega}_l} q d\Omega. \quad (5)$$

for all $l \in [1, M]$. With the Gauss theorem one obtains

$$-\int_{\partial\bar{\Omega}_l} \left(\lambda \cdot \sum_{h=1}^N \left(\sum_{k=1}^M \bar{p}_k \nabla \Phi_k^h + \nabla \Phi^h \right) \right) \cdot \tilde{\mathbf{n}}_l d\Gamma = \sum_{k=1}^M \bar{p}_k \sum_{h=1}^N \int_{\partial\bar{\Omega}_l} (-\lambda \cdot \nabla \Phi_k^h) \cdot \tilde{\mathbf{n}}_l d\Gamma + \sum_{h=1}^N \int_{\partial\bar{\Omega}_l} (-\lambda \cdot \nabla \Phi^h) \cdot \tilde{\mathbf{n}}_l d\Gamma = \int_{\bar{\Omega}_l} q d\Omega, \quad (6)$$

which results in the linear system

$$A_{lk} \bar{p}_k = b_l \quad (7)$$

for \bar{p}_k with

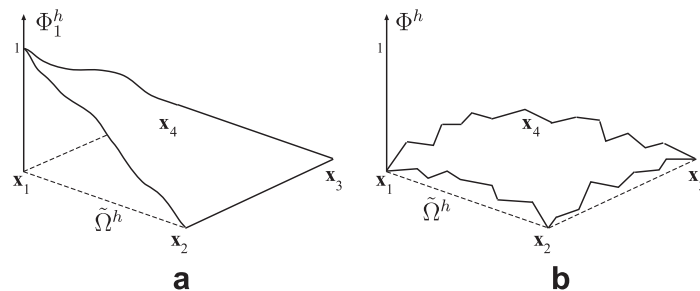


Fig. 2. Illustration of the basis function Φ_1^h (a) and correction function Φ^h (b).

$$A_{lk} = \sum_{h=1}^N \int_{\partial\bar{\Omega}_l} (-\lambda \cdot \nabla \Phi_k^h) \cdot \bar{\mathbf{n}}_l d\Gamma \quad (8)$$

and

$$b_l = \int_{\bar{\Omega}_l} q d\Omega - \sum_{h=1}^N \int_{\partial\bar{\Omega}_l} (-\lambda \cdot \nabla \Phi^h) \cdot \bar{\mathbf{n}}_l d\Gamma. \quad (9)$$

The unit normal vector $\bar{\mathbf{n}}_l$ points out of $\bar{\Omega}_l$. Note that the right-hand side b_l also contains the effects of the fine-scale fluxes across $\partial\bar{\Omega}_l$ induced by the correction functions Φ^h .

With \bar{p}_k and the superposition (2) one obtains the fine-scale pressure p' , which is an approximation of the fine-scale reference solution p_f . An interesting property of this MSFV method is that the difference between p' and p_f is solely due to the localization assumption (4), i.e. with

$$r^h = (\bar{\mathbf{n}}^h \cdot \nabla)((\lambda \cdot \nabla p_f) \cdot \bar{\mathbf{n}}^h) \quad \text{at} \quad \partial\bar{\Omega}^h \forall h \in [1, N] \quad (10)$$

the two fine-scale pressure fields become identical.

It has been shown for a wide range of challenging test cases that the MSFV method with $r^h = 0$ leads to very accurate results. In other words: in general, the reduced problem boundary conditions provide a good localization assumption.

For multiphase problems, a conservative fine-scale velocity field is required to honor mass balance of the transported phase saturations. While the velocity

$$\mathbf{u}' = -\lambda \cdot \nabla p' \quad (11)$$

fulfills this requirement in a weak sense, i.e. for each coarse volume $\bar{\Omega}_k$, it is non-conservative at the fine-scale. Therefore, if one is interested in solving saturation transport on the fine grid, a further step is required. To reconstruct a conservative fine-scale velocity field \mathbf{u}'' , which is consistent with \mathbf{u}' , the additional local problems

$$-\nabla \cdot (\lambda \cdot \nabla p_k'') = q \quad \text{on} \quad \bar{\Omega}_k \quad (12)$$

with

$$(\lambda \cdot \nabla p_k'') \cdot \bar{\mathbf{n}}_k = (\lambda \cdot \nabla p') \cdot \bar{\mathbf{n}}_k \quad \text{at} \quad \partial\bar{\Omega}_k \quad (13)$$

are solved. Note that the velocity field

$$\mathbf{u}'' = \begin{cases} -\lambda \cdot \nabla p_k'' & \text{on } \bar{\Omega}_k \\ -\lambda \cdot \nabla p' & \text{at } \partial\bar{\Omega}_k \end{cases} \quad (14)$$

for all $k \in [1, M]$ is conservative (provided p'' is obtained with a conservative scheme) and can be employed to solve transport equations on the fine grid [10]. For multiphase subsurface flow problems, for example, saturation transport may be calculated explicitly [22] or implicitly [23]. Since the mobility λ generally depends on the saturations, in the implicit version one has to iterate between the pressure equation (1), which is solved with the MSFV method, and the transport equations. Good efficiency is achieved, if the latter one is solved implicitly on the individual domains $\bar{\Omega}_k$. The local solutions are then coupled by a simple Schwarz overlap scheme [23,24]. With this technique, which is very efficient for hyperbolic problems, the low computational complexity of the overall MSFV algorithm can be maintained for multiphase flow.

An important property of the MSFV method is its adaptivity. For example, the conservative velocity reconstruction described above is only required in those coarse cells $\bar{\Omega}_k$ where fine-scale transport is of interest. Moreover, very importantly, the basis and correction functions can be stored and reused for subsequent time steps. They have to be recomputed only in those dual cells $\bar{\Omega}^h$ where changes of the coefficient λ or (for the correction functions) the right-hand side q exceed a specified limit [22,23,25]. Recently, in order to make the MSFV method applicable for realistic problems, it was extended to include compressibility [26–28], gravity [27,29–32], and complex wells [33–35]. All these extended versions of the MSFV method proved to be very effective for a wide range of challenging cases for which the multiscale and fine-scale solutions are in excellent agreement. There exist scenarios, however, which demonstrate some limitations of the MSFV method. One involves extended structures with sharp mobility contrasts. Examples are extended and almost impermeable shale layers [17], and meanders as they exist in the bottom layers of the SPE comparative test case 10 [36]. Another class of problems for which the MSFV method fails to give accurate solutions are cases with large coarse-cell aspect ratios or highly anisotropic mobilities. Although various ways to overcome this problem have been devised [37,16], there still exists potential for improvement. Finally, it would be of great interest to have a method, which allows to improve the local pressure field iteratively to any desired level.

Next, we present an extension, which allows to iteratively improve MSFV solutions. It will be shown that the fine-scale reference solutions can be recovered even for those cases mentioned above, where the standard MSFV method experiences difficulties.

3. Iterative MSFV (i-MSFV) method

As already pointed out, the difference between the MSFV solution p' and the fine scale reference pressure p_f is solely due to the localization assumptions, i.e. p' and p_f become identical if the boundary conditions (4) are employed in fulfillment of requirement (10) for r^h . Unfortunately, however, Eq. (10) requires a priori knowledge of p_f .

3.1. Algorithm

Here, we explain a convergent iterative procedure to improve the localization boundary conditions, which does not depend on p_f .

Instead of requirement (10), we consider the iterative improvement

$$r^{h(t)} = (\tilde{\mathbf{n}}^h \cdot \nabla)((\lambda \cdot \nabla p_s^{(t)}) \cdot \tilde{\mathbf{n}}^h) \quad \text{at} \quad \partial\tilde{\Omega}^h \forall h \in [1, N] \quad (15)$$

of r^h . The superscript (t) denotes the iteration level and

$$p_s^{(t)} = S^{n_s} \cdot p^{(t)} + T = S^{n_s} \cdot \sum_{h=1}^N \left[\sum_{k=1}^M \Phi_k^h \bar{p}_k^{(t)} + \Phi^{h(t-1)} \right] + T \quad (16)$$

is the smoothed MSFV fine-scale pressure approximation, where S is a linear smoothing operator, T is the non-homogeneous part of the iterative smoother, and n_s the number of smoothing steps. Note that the correction functions $\Phi^{h(t-1)}$ are based on the local boundary conditions (4) with $r^h = r^{h(t-1)}$.

For a more compact presentation of the iterative MSFV (i-MSFV) method, we order the fine-grid values of p'_s , p' , Φ_k^h , and Φ^h in vectors \mathbf{p}'_s , \mathbf{p}' , Φ_k^h , and Φ^h with entries $[p'_s]_i$, $[p']_i$, $[\Phi_k^h]_i$, and $[\Phi^h]_i$, respectively. We then express in matrix form all linear equations involved in the iterative procedure described above and write

$$[\Phi^{h(t-1)}]_i = C_{ij}^h [p_s^{(t-1)}]_j + E_i^h, \quad (17)$$

$$A_{lk} \bar{p}_k^{(t)} = \underbrace{Q_l}_{\int_{\bar{\Omega}_l} q d\Omega} + \underbrace{D_{li} [\Phi^{h(t-1)}]_i}_{-\sum_{h=1}^N \int_{\partial\bar{\Omega}_l} (-\lambda \cdot \nabla \Phi^{h(t-1)}) \cdot \bar{\mathbf{n}}_l d\Gamma}, \quad (18)$$

$$[p_s^{(t)}]_i = [S^{n_s}]_{ij} \sum_{h=1}^N ([\Phi_k^h]_j \bar{p}_k^{(t)} + [\Phi^{h(t-1)}]_j) + T_i. \quad (19)$$

Eq. (17) corresponds to the localized problems for the correction functions $\Phi^{h(t-1)}$, as following from the original elliptic Eq. (1) with the boundary condition (4) defined according to (15). The terms on the right-hand side express the linear dependence of $\Phi^{h(t-1)}$ on the smoothed pressure field $p_s^{(t-1)}$ at the previous iteration step (due to the iterative boundary condition (15)) and on the source term q of the elliptic problem, respectively. Eq. (18) corresponds to the coarse-scale problem (5), and is equivalent to Eqs. (7)–(9). Finally, Eq. (19) expresses the iterative reconstruction formula (16). Combining Eqs. (17)–(19) and indicating with \mathbf{I} the identity matrix, we obtain the linear relation

$$[p_s^{(t)}]_i = \underbrace{[S^{n_s}]_{ij} \sum_{h=1}^N [[\Phi_k^h]_j A_{kl}^{-1} (Q_l + D_{lq} E_q^h) + E_j^h] + T_i}_{b_i^{(t)}} + \underbrace{[S^{n_s}]_{ij} \sum_{h=1}^N [([\Phi_k^h]_j A_{kl}^{-1} D_{lq} + I_{jq}) C_{qr}^h] [p_s^{(t-1)}]_r}_{A_{iq}^{(n_s)}} \quad (20)$$

between the smoothed fine-scale pressure fields $p_s^{(t-1)}$ and $p_s^{(t)}$, at two consecutive iteration steps.

An algorithmic outline of the i-MSFV method is shown in Table 1. First, the fine-scale pressure is initialized, e.g. it is set to zero. Then, all basis functions are computed and the right-hand side of the elliptic pressure equation is integrated over each coarse volume. These steps have to be performed only once and are followed by the main iteration loop. At the beginning of each iteration, n_s smoothing steps are applied and the smoothed fine-scale pressure is employed to compute the correction functions. These are required to obtain the right-hand side of the linear system for the coarse pressure. At the end of each iteration, the coarse system is solved and the new fine-scale pressure approximation is reconstructed. Note that the components of the vector \mathbf{p} are the actual pressure values at the dual coarse-grid nodes.

3.2. Interpretation as a multigrid method

The operations depicted in Table 2 illustrate how the i-MSFV algorithm can be interpreted as a multigrid method. First, n_s smoothing steps (iterative linear solver) are applied to improve the approximate fine-grid solution $\mathbf{p}^{(t-1)}$. A subsequent restriction step leads to the right-hand side $\mathbf{b}^{(t-1)}$ of the coarse-grid system for the pressure values $\bar{\mathbf{p}}^{(t)}$ at the dual coarse-grid nodes. Note that this involves updating the correction functions $\Phi^{h(t-1)}$; the coarse-grid operator \mathbf{A} on the other hand, which is based on the basis functions Φ_k^h , has to be constructed only once at the beginning. The coarse system can be solved with any suitable solver, but due to the typically extreme coarsening factors, the coarse problem may be small enough to be solved directly. The

Table 1

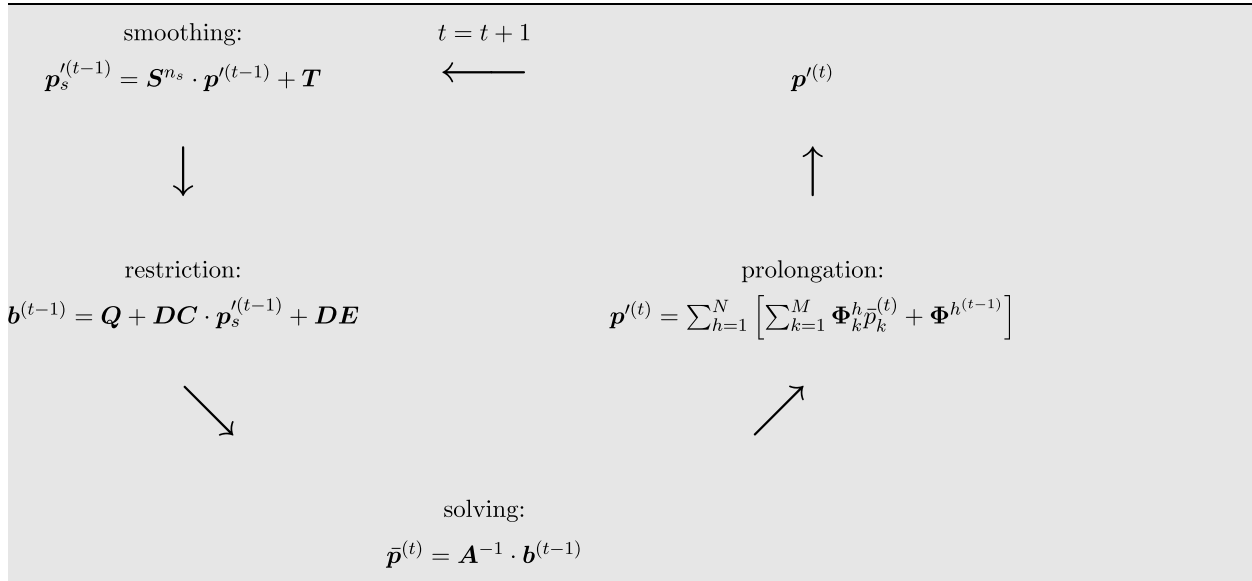
Algorithmic outline of the i-MSFV method

```

initialize  $\mathbf{p}^{(t=0)}$ 
 $\forall h : \forall k$  : compute basis functions  $\Phi_k^h$ 
calculate  $\mathbf{Q}$ ; Eq. (18)
for  $t = 1$  to number of i-MSFV iterations {
   $\mathbf{p}_s^{(t-1)} = \mathbf{p}^{(t-1)}$ 
  for  $i = 1$  to  $n_s$  {
     $\mathbf{p}_s^{(t-1)} = \mathbf{S} \cdot \mathbf{p}_s^{(t-1)} + \mathbf{T}$ ; smoothing step
  }
   $\forall h$  : compute correction function  $\Phi^{h(t-1)}$ ; based on  $\mathbf{p}_s^{(t-1)}$ 
  calculate  $\mathbf{b}^{(t-1)} = \mathbf{Q} + \mathbf{DC} \cdot \mathbf{p}_s^{(t-1)} + \mathbf{DE}$ ; Eq. (18)
  solve coarse system  $\mathbf{A} \cdot \bar{\mathbf{p}}^{(t)} = \mathbf{b}^{(t-1)}$ ; Eq. (18)
  reconstruct  $\mathbf{p}^{(t)}$ ; Eq. (2)
}
```

Table 2

The i-MSFV algorithm interpreted as a multigrid method



updated fine-grid solution $\mathbf{p}^{(t)}$ is obtained by prolongation, which is simply achieved by superimposing the correction functions plus the basis functions weighted with the new coarse pressure values. Note that this interpretation of the i-MSFV method as a multigrid method is different than what is presented in [28], where no correction functions are considered there.

Although only shown here for two grid levels, the i-MSFV method can be extended for more complex cycles. Moreover, it can be seen from the abstract operations in Tables 1 and 2 that no assumptions regarding the topologies of the fine- and coarse-scale grids are required. For example, the same methodology can be applied for unstructured fine grids, and instead of coarse grids one can employ appropriate domain decompositions. In any case, however, the smoothing scheme is critical for robustness and good convergence. For all the cases we considered it was found that consistent line-relaxation works very well (note that a different smoother would be required for unstructured fine grids). This might be mainly due to the effectiveness of line-relaxation to distribute the residuum from the coarse dual-cell boundaries across the domain. Moreover, line-relaxation only depends weakly on the grid aspect ratio and on the level of anisotropy [38]. Next, the line relaxation scheme used for the studies presented in this paper is described.

3.3. Fine-scale smoothing

As already mentioned, line-relaxation (LR) is only one possibility to smooth the approximate fine-grid solution $\mathbf{p}^{(t-1)}$. Here, we describe how LR is employed in our current i-MSFV implementation. Therefore, we consider the fine-scale system

$$\mathbf{M} \cdot \mathbf{p}_f = \mathbf{R}, \quad (21)$$

which results form a conservative finite-volume discretization of Eq. (1) on the fine grid. For simplicity we assume that the grid lines are parallel to the x -, y - and z -directions of a Cartesian coordinate system. The extension of this algorithm to unstructured grids is a topic of future research and not within the scope of this paper. Then we split the linear operator

as $\mathbf{M} = \mathbf{M}_x + \mathbf{M}_y + \mathbf{M}_z$, where $\mathbf{M}_{x,y,z}$ represent the discretizations of the elliptic operator in the corresponding coordinate directions. If only one operator plus the diagonal components of the other ones are treated implicitly, one obtains the iterative scheme

$$(\mathbf{M}_x + \text{diag}(\mathbf{M}_y + \mathbf{M}_z)) \cdot \mathbf{p}^{v+1/3} = \mathbf{R} - (\mathbf{M}_y + \mathbf{M}_z - \text{diag}(\mathbf{M}_y + \mathbf{M}_z)) \cdot \mathbf{p}^v, \quad (22)$$

$$(\mathbf{M}_y + \text{diag}(\mathbf{M}_x + \mathbf{M}_z)) \cdot \mathbf{p}^{v+2/3} = \mathbf{R} - (\mathbf{M}_x + \mathbf{M}_z - \text{diag}(\mathbf{M}_x + \mathbf{M}_z)) \cdot \mathbf{p}^{v+1/3}, \quad (23)$$

$$(\mathbf{M}_z + \text{diag}(\mathbf{M}_x + \mathbf{M}_y)) \cdot \mathbf{p}^{v+1} = \mathbf{R} - (\mathbf{M}_x + \mathbf{M}_y - \text{diag}(\mathbf{M}_x + \mathbf{M}_y)) \cdot \mathbf{p}^{v+2/3}, \quad (24)$$

where \mathbf{p}^v is the approximate solution after the v th LR-step and $\text{diag}(\mathbf{M}_x)$ represents the matrix with the diagonal of \mathbf{M}_x . This scheme, in which the three linear systems (22)–(24) are solved sequentially each iteration, is a slightly modified version of the alternating directions implicit (ADI) method by Peaceman and Rachford [39]. For a two-point flux approximation, the linear operators $\mathbf{M}_{x,y,z}$ have a tri-diagonal structure and the systems (22)–(24) can be solved with the Thomas algorithm [40], which has a linear complexity. Moreover, these three operators can further be split into independent linear systems for each grid line, which is an important property for massive parallel computing. Note that this iterative LR solver is convergent, but for big problems the rate is extremely slow. In our framework, however, only very few LR-steps are required to smooth $\mathbf{p}^{(t-1)}$ sufficiently for an effective improvement of the local boundary conditions. As demonstrated in Section 4, the optimum number of smoothing steps per i-MSFV iteration is case dependent.

4. Numerical convergence studies

Here, the convergence rate of the i-MSFV method is assessed. The first set of studies is based on a test case consisting of a rectangular 2D domain with constant pressure and no-flow conditions at the vertical and horizontal boundaries, respectively. For the discretization, an equidistant Cartesian fine grid with 44×44 cells was used and in addition, for the i-MSFV method, a 4×4 coarse grid was employed (Fig. 3(a)). Since each coarse cell is composed of 11×11 fine cells, the upscaling factor is 11 in each coordinate direction. For the following studies, homogeneous and heterogeneous mobility fields and domains with different aspect ratios α (horizontal to vertical dimension) are considered. The size of each fine cell is $\Delta x \times \Delta y$ with $\Delta x = 1 = \alpha \Delta y$. Note that a case with isotropic mobility and $\Delta x = \alpha \Delta y$ is numerically identical to a case with $\Delta x = \Delta y$ and a mobility which is larger by a factor of α^2 in the y -direction.

The homogeneous test cases with $\lambda_{ij} = \delta_{ij}$ also include a source with $q = 1/(\Delta x \Delta y)$ and a sink with $q = -1/(\Delta x \Delta y)$ distributed over the fine cells (13, 13) and (32, 32), respectively (Fig. 3(a)). For the heterogeneous cases, the mobility field depicted in Fig. 3(b) with natural logarithm (ln) variance and mean of 6.66 and -0.29 , respectively, which is a part of the top layer of the three-dimensional SPE10 test case [36], was used.

Fig. 4 shows the base-10 logarithm (log) of the maximum error in the domain, i.e. $\log(\epsilon)$ with $\epsilon = \|p' - p_f\|_\infty$, as a function of i-MSFV iterations and smoothing steps (per iteration), n_s , for the homogeneous (Fig. 4(a) and (c)) and heterogeneous (Fig. 4(b) and (d)) cases with $\alpha = 1$ (Fig. 4(a) and (b)) and $\alpha = 10$ (Fig. 4(c) and (d)). For all cases there exists a minimum n_s , for which the i-MSFV method converges. The best convergence can be observed for the homogeneous isotropic ($\alpha = 1$) case and the worst convergence for the heterogeneous case with $\alpha = 10$.

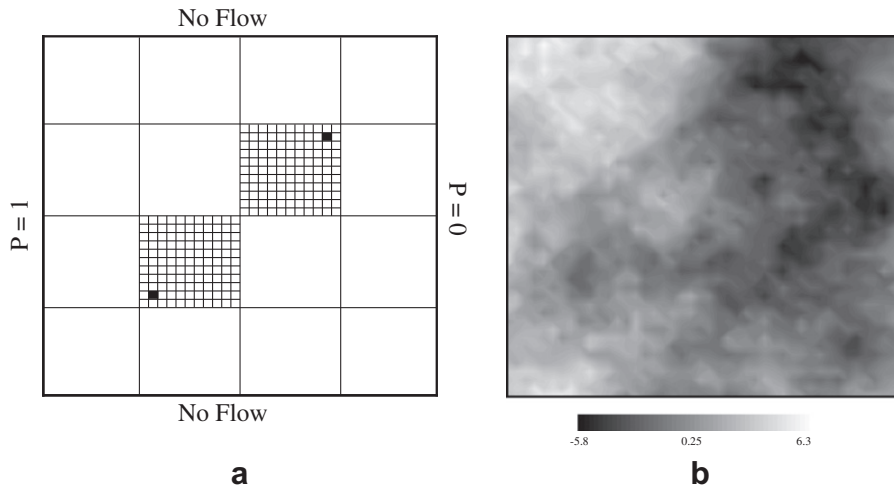


Fig. 3. (a) computational domain, which consists of 44×44 fine and 4×4 coarse cells. In the homogeneous cases, the fine cells marked black contain a source and a sink of strength $1/(\Delta x \Delta y)$ and $-1/(\Delta x \Delta y)$, respectively and (b) natural logarithm of the heterogeneous mobility field.

Fig. 5(a) shows the convergence histories for the heterogeneous test case as a function of α with $n_s = 10$. The slope decreases as α increases, but eventually it approaches an asymptotic value. This observation is confirmed by the plot in Fig. 5(b), which shows the convergence rate (average slope between $\log(\epsilon) = -2$ and $\log(\epsilon) = -6$) as a function of α and n_s for the heterogeneous-anisotropic case. For $\alpha \geq 20$, the convergence dependence on the aspect ratio becomes negligible. This result is encouraging, since it demonstrates that the i-MSFV method can be applied for cases with very large aspect ratios and/or extreme anisotropies. One reason for this is the following property of the LR solver, which acts as a smoother in the i-MSFV method. For comparison, Fig. 5(b) also shows the convergence rates (multiplied with 100) of the LR solver for cases with different aspect ratios. Note that virtually no sensitivity on α can be detected.

Fig. 6(a) illustrates how the convergence rate increases with n_s . To estimate the optimal number of smoothing steps per iteration, we assume that the amount of computational work to calculate the correction functions, to solve the coarse problem, and to reconstruct p' corresponds to β times the computational work required for one smoothing step. This leads to the

$$\text{Effective convergence rate} = \frac{\text{Convergence rate}}{1 + n_s/\beta}. \quad (25)$$

It is a measure for the error reduction, if the computational work equivalent to one MSFV iteration (without smoothing nor reconstruction of a conservative velocity field) is invested. Fig. 6(b) shows the effective convergence rates for various aspect ratios α as functions of n_s , where β is assumed to be one.

To analyze the computational cost associated with the i-MSFV method as a function of the problem size, the number of fine cells in the homogeneous isotropic test case was increased successively by adding coarse-grid cells with 11×11 fine cells each. Fig. 7 depicts the convergence rates for 2×2 , 3×3 , 4×4 , 5×5 , 6×6 , 7×7 , 8×8 , 9×9 , and 10×10 coarse grids, and the log – log plot clearly shows (dashed line) that the convergence rate (for constant $n_s = 10$) is insensitive to

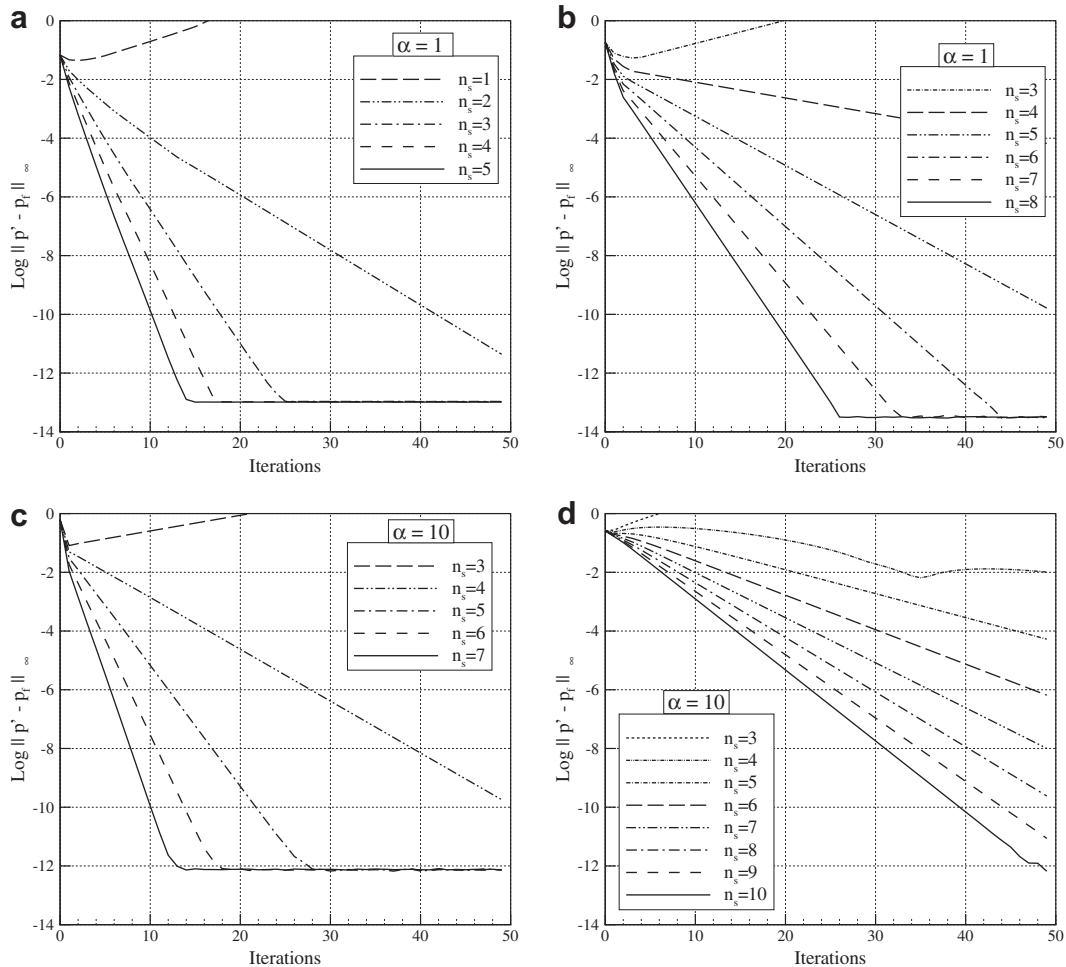


Fig. 4. Numerical convergence study with the first set of test cases: (a) homogeneous-isotropic, (b) heterogeneous-isotropic, (c) homogeneous-anisotropic ($\alpha = 10$) and (d) heterogeneous – anisotropic ($\alpha = 10$).

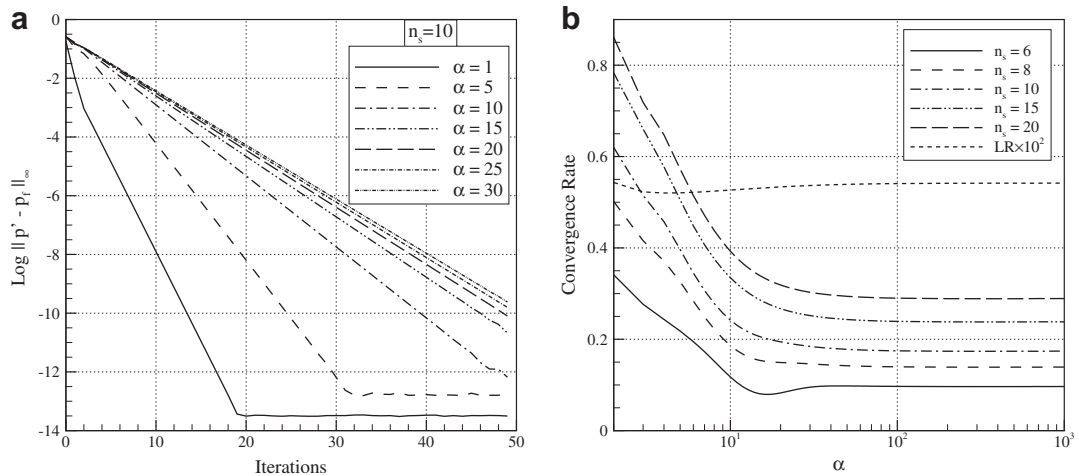


Fig. 5. (a) convergence history of the i-MSFV method for the heterogeneous domain with $n_s = 10$ and different aspect ratios and (b) convergence rates of the pure LR solver (multiplied by 100) and the i-MSFV method for the heterogeneous, anisotropic domain with different n_s as a function of the aspect ratio.

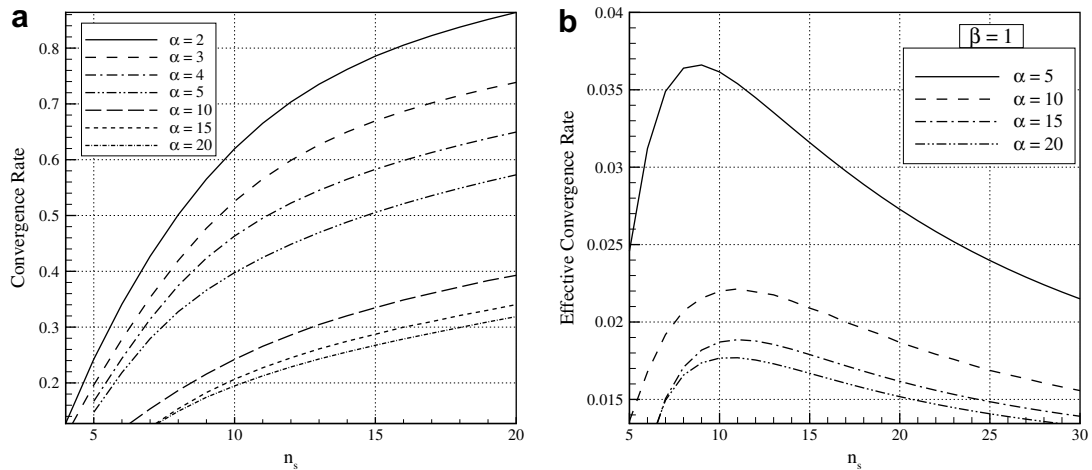


Fig. 6. (a) effect of n_s on the convergence rate of the i-MSFV method for the heterogeneous domain with different aspect ratios and (b) effective convergence rate for heterogeneous-anisotropic test cases.

the fine-grid size; opposed to the convergence rate of the LR-solver (solid line). Moreover, all calculation steps in the i-MSFV algorithm, except solving the global coarse-scale problem, can be performed locally and independently. Therefore, since up to very large cases the cost for solving the coarse system is virtually negligible, the i-MSFV algorithm is a very efficient linear solver for large, stiff problems, and it is ideally suited for massive parallel computing.

Another interesting parameter is the upscaling factor. Fig. 8 shows the convergence rate for the heterogeneous case with upscaling factors Γ of 11×11 , 7×7 , and 5×5 . In Fig. 8(a), the convergence rates are shown as functions of α with constant $n_s = 10$ and in Fig. 8(b), they are depicted as functions of n_s with constant $\alpha = 5$. Obviously, the optimal choice of Γ depends on the size of the fine grid and on the computational cost of the individual algorithmic components; in particular of the coarse-scale solver.

To complete our numerical investigations of the i-MSFV convergence behavior, four sets of 20 realisations of log-normally distributed mobility fields with spherical variogram and dimensionless correlation lengths $\psi_1 = 0.5$ and $\psi_2 = 0.02$ are generated using sequential Gaussian simulations [41]. For each set, variance and mean of $\ln(\lambda)$ are 2.0 and 3.0, respectively. As depicted in Fig. 9, the angles θ between the long correlation length and vertical domain boundaries (or vertical grid lines orientation) are 0° , 15° , 30° , and 45° . For each case, a 100×100 fine and a 20×20 coarse grid were employed. At the boundaries of the quadratic domain, no-flow conditions were applied and at the lower left and upper right corners (cells (3,3) and (97,97)), a source and a sink of equal strength ($q = \pm 1/(\Delta x \Delta y)$) were imposed (Fig. 10). Fig. 11(a) and (b) shows the mean convergence rates as functions of θ for different n_s , α , and Γ . As one can see, there is a significant difference in the convergence rates. However, in general the convergence rate decreases with increasing layering orientation angle θ .

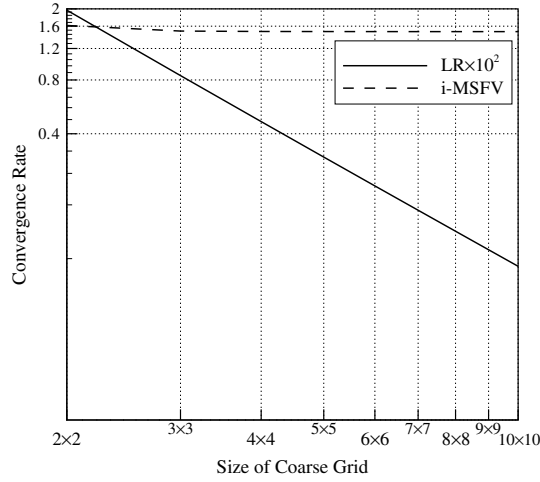


Fig. 7. Effect of domain size on the convergence rate of the i-MSFV method with $n_s = 10$ and on the convergence rate of LR (multiplied by 100) for the homogeneous-isotropic domain.

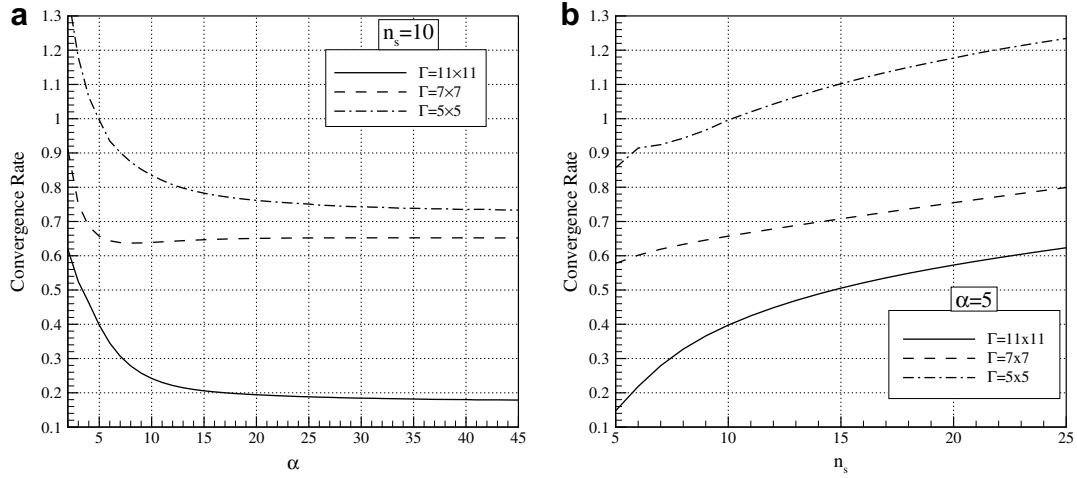


Fig. 8. Convergence rate of the i-MSFV method for a heterogeneous domain versus aspect ratio (a) and number of smoothing steps (b) for different upscaling factors.

5. Spectral analysis of the i-MSFV method

We conclude the convergence assessment of the i-MSFV method by analysing the spectrum of the associated iteration matrix, i.e., according to Eq. (20), of $\mathbf{A}^{*(n_s)}$ in

$$\mathbf{p}_s^{(t)} = \mathbf{A}^{*(n_s)} \cdot \mathbf{p}_s^{(t-1)} + \mathbf{b}^*. \quad (26)$$

Clearly, the iteration procedure converges, if and only if all eigenvalues of $\mathbf{A}^{*(n_s)}$ lay within the unit-disc of the complex plane.

Various spectra of $\mathbf{A}^{*(n_s)}$ for the homogeneous anisotropic test case with no-flow conditions at all boundaries are depicted in Fig. 12. Fine and coarse grids consist of 44×44 and 4×4 cells, respectively and the different figures refer to iteration matrices based on different n_s . These results confirm those presented in Fig. 4(a), according to which at least two smoothing steps are required for the homogeneous isotropic case. Notice that unlike the matrix \mathbf{M} of the fine-scale problem (21), $\mathbf{A}^{*(n_s)}$ is not symmetric and possesses non-real eigenvalues. All eigenvalues of $\mathbf{A}^{*(n_s)}$ are clustered around the negative real axis, which implies that the approximate solution at successive iteration steps oscillates around the exact one.

The eigenfunctions \tilde{p} associated with the largest eigenvalues are plotted in Fig. 13 together with the corresponding residuum $\rho = \nabla \cdot \lambda \cdot \nabla \tilde{p}$ in the discrete fulfillment of Eq. (1) without right-hand side. Only the results for $n_s = 0$ (unstable) and

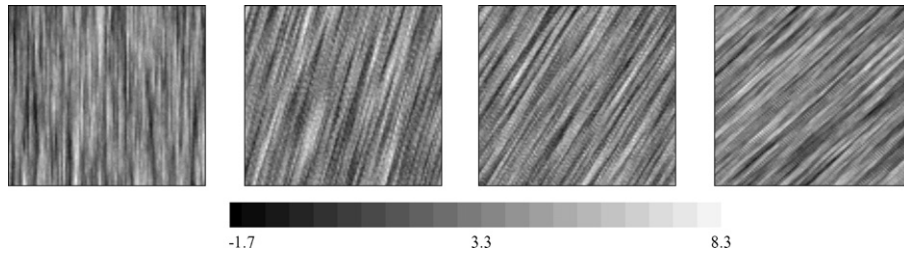


Fig. 9. Natural logarithm of one of the 20 different mobility field realizations used in this study (for different angles $\theta = 0^\circ$, $\theta = 15^\circ$, $\theta = 30^\circ$, and $\theta = 45^\circ$ from left to right).

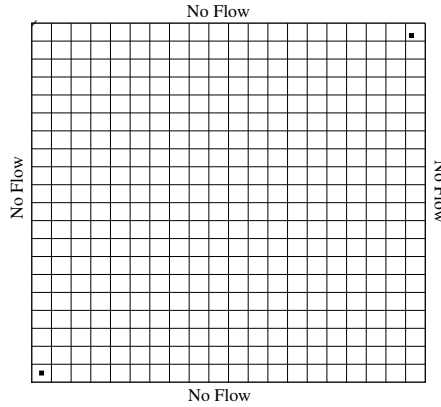


Fig. 10. Computational domain, which consists of 20×20 coarse cells (shown); each coarse cell contains 5×5 fine cells (not shown). The black squares mark the two wells with $q = \pm 1/(\Delta x \Delta y)$ distributed over the fine cells (3,3) and (97,97).

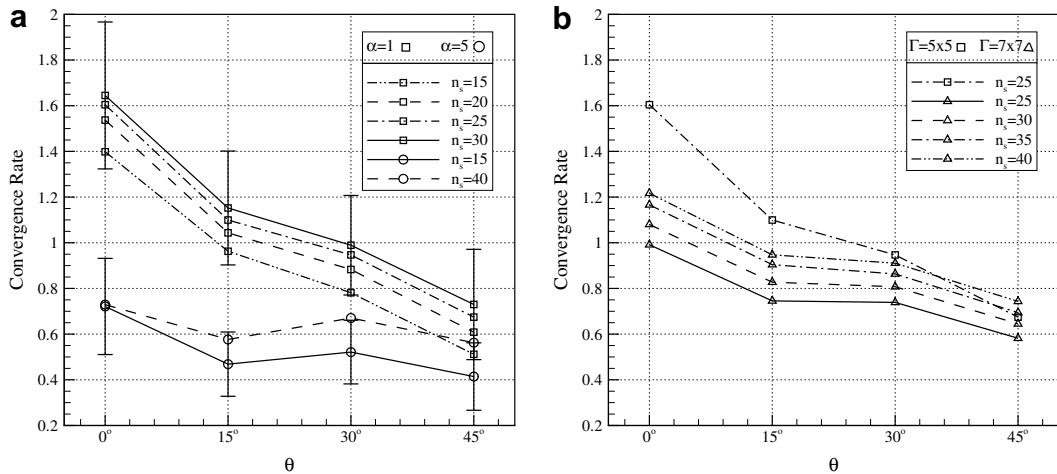


Fig. 11. (a): mean convergence rate for different angles θ , different numbers of smoothing steps, and $\Gamma = 5 \times 5$. Also shown are the error bars for the two test cases. (b): convergence rate for two different upscaling factors of 5×5 and 7×7 . The convergence rate for $\Gamma = 7 \times 7$ is presented for different smoothing steps.

$n_s = 2$ (stable) are shown. In both cases, the residuum is largest at the dual-cell boundaries and without smoothing it is zero everywhere else. This is in agreement with the fact that any non-smoothed solution p' fulfills Eq. (1) exactly inside the coarse dual cells. The smoothing steps efficiently redistribute the residuum and reduce its maximum amplitude. Consequently, the eigenvectors of $\mathbf{A}^{(n_s)}$ get amplified for $n_s = 0$ and damped for $n_s = 2$.

In Fig. 14, similar spectra of the iteration matrix $\mathbf{A}^{(n_s)}$ can be observed for cases with heterogeneous mobility fields. In Fig. 15(a) and (b), the largest values of the residua associated with the ten least stable eigenvectors for $n_s = 0$ and $n_s = 5$, respec-

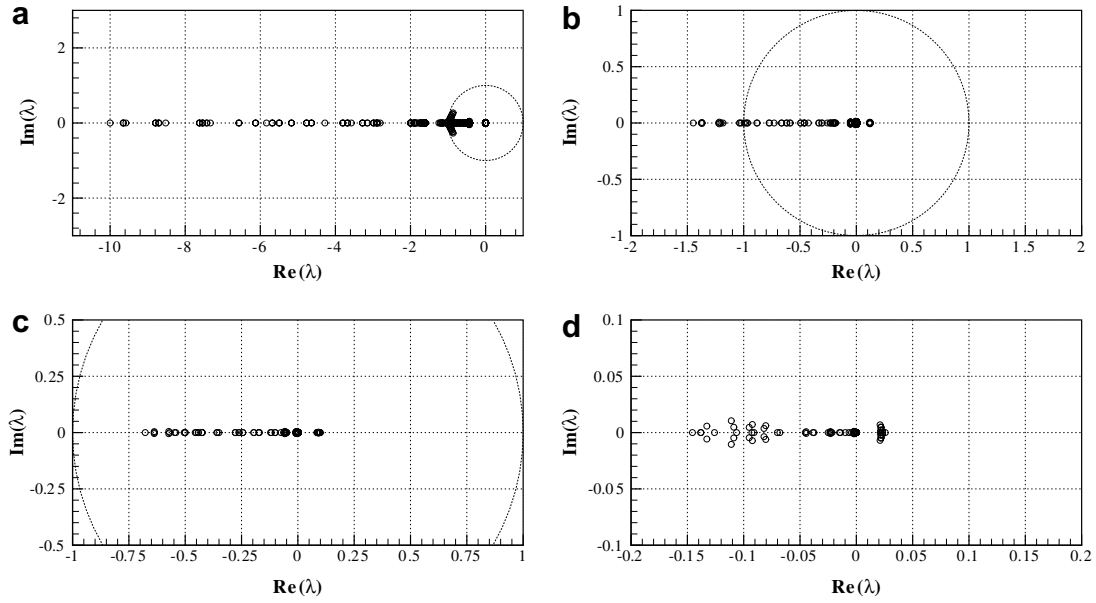


Fig. 12. Spectra of the iteration matrix $\mathbf{A}^{(n_s)}$ of i-MSFV method for the homogeneous isotropic case with 44×44 fine cells, 4×4 coarse cells, no-flow boundary conditions at $\partial\Omega$ and different values for n_s : (a) $n_s = 0$, (b) $n_s = 1$, (c) $n_s = 2$ and (d) $n_s = 5$.

tively, are presented. Notice the discontinuous distribution in Fig. 15(a) for the case with $n_s = 0$. Clearly, the residuum gets distributed by the $n_s = 5$ smoothing steps (Fig. 15(b)). Finally, Fig. 16(a) and (b) depict the least stable eigenvector for $n_s = 5$ and its residuum.

6. Application to subsurface flow

In typical incompressible subsurface flow simulations, the pressure in the porous media is governed by Eq. (1). As in the examples of Section 4, the mobility λ typically has a complex distribution with high variance and sharp contrasts. It is a function of the rock permeability \mathbf{k} , the fluid phase saturations and the fluid viscosities. For single-phase flow of a fluid with viscosity μ one can write $\lambda = \mathbf{k}/\mu$. The expression for multiphase flow is based on the relative permeability concept and reads $\lambda = \mathbf{k} \sum_{j=1}^{n_p} k_{rj}/\mu_j$ (n_p is the number of fluid phases). The relative permeabilities k_{rj} [40] have to be specified for each fluid phase j as functions of the saturations. While λ does not change with time in single-phase flow simulations, it evolves if multiple fluid phases are transported through the reservoir. For the following studies, the right-hand side of Eq. (1) is non-zero only at the well, i.e. no capillary pressure difference between the fluid phases and no gravity are considered.

6.1. Single-phase flow

Here, in addition to the examples discussed in Section 4, the convergence behavior of the i-MSFV method for single-phase flow in particularly challenging reservoirs is investigated. The rectangular 2D domain is discretized by a Cartesian, equidistant 220×55 fine grid. No-flow conditions are applied at the bottom and top walls; at the left and right boundaries, constant dimensionless pressure values of 1 and 0 are applied, respectively. The convergence histories for the permeability fields from the top and bottom layers (Fig. 17(a) and (b)) of the 3D SPE 10 test case [36] are shown in Fig. 18(a) and (b), respectively, where a 20×5 coarse grid was employed. As previously, the error is defined as the logarithm of the maximum absolute difference between the approximate i-MSFV and the reference fine-scale pressure values. While for the top layer a good convergence rate is achieved with $n_s = 10$ (Fig. 18(a)), approximately 250 smoothing steps are required for optimal convergence with the bottom layer permeability field (Fig. 18(b)). However, also in this case many more smoothing steps are necessary, if LR is employed as an iterative linear solver ($\sim 10^5$ iterations are necessary in order to reduce the error by 5 orders of magnitude). Moreover, Fig. 19 illustrates that the number of smoothing steps can be reduced dramatically, if a coarsening factor of $\Gamma = 5 \times 5$ (and fine grid of 220×60) instead of $\Gamma = 11 \times 11$ (and fine grid of 220×55) is employed.

As a further test case, a rectangular domain with two almost impermeable shale layers is considered (Fig. 20(a)); the mobility in the shale layers is 10^{10} times smaller than in the rest of the domain. The equidistant Cartesian fine grid consists of 55×55 cells and the coarse grid for the i-MSFV method contains 5×5 volumes. Again, no-flow conditions are applied at the bottom and top boundaries and at the left and right sides the dimensionless pressure values are set equal to 1 and 0, respectively. Fig. 20(b) shows the convergence histories with $n_s = 10$ for different aspect ratios.

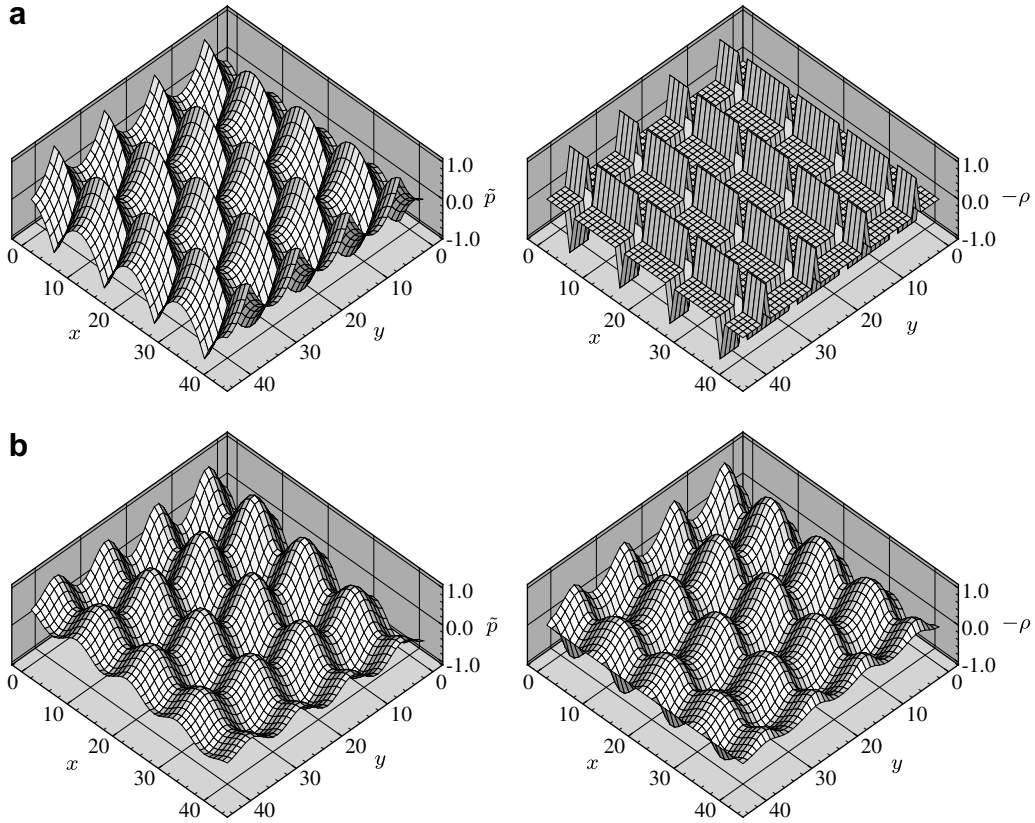


Fig. 13. Eigenvectors associated to the largest eigenvalues of the spectra from Fig. 12 (left) and corresponding residuum in the fulfillment of Eq. (1) (right) without right-hand side: (a) $n_s = 0$ and (b) $n_s = 2$. Eigenvectors and residua are independently rescaled.

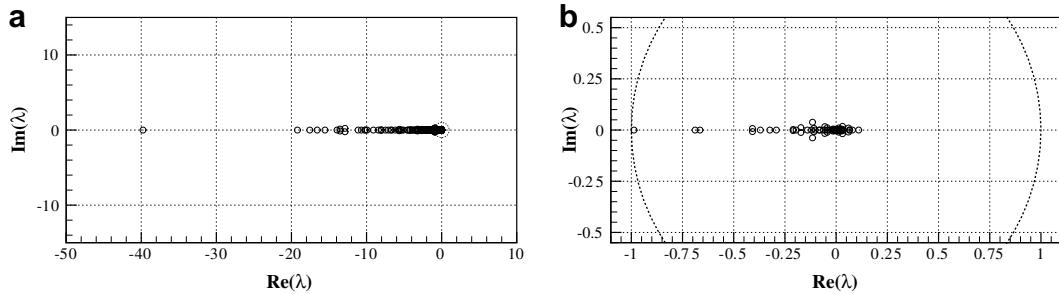


Fig. 14. Spectra of the iteration matrix $\mathbf{A}^{(n_s)}$ for the heterogeneous isotropic case with 44×44 fine cells, 4×4 coarse cells, no-flow boundary conditions on $\partial \Omega$ and different values for n_s : (a) $n_s = 0$ and (b) $n_s = 5$.

6.2. Multi-phase flow

As already pointed out, in multiphase flow simulations the mobility λ and therefore the pressure field evolve with time as the phase saturations are transported through the domain. Obviously, this also affects the localization boundary conditions, which continuously experience changes in the whole domain, even where the mobility remains constant. Consequently, in a straight forward application of the i-MSFV method for multiphase flow, all correction functions have to be re-computed multiple times every time-step. Although the number of i-MSFV iterations is reduced by the good initial condition obtained from the previous time step, such an approach is significantly more expensive than the original MSFV method. Here it is shown that only infrequently updating the localization boundary conditions for the re-computation of the correction functions is sufficient to obtain highly accurate solutions. While at the beginning of a simulation a converged solution is computed, the same localization boundary conditions are used for a number of subsequent time steps and are only updated infrequently, e.g. each 10th time step by applying one iteration. Therefore, for the major part of the simulation the original MSFV

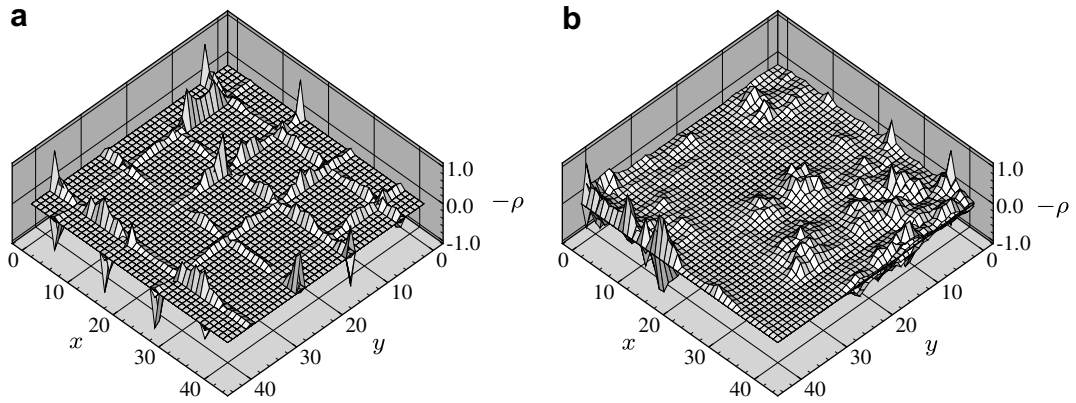


Fig. 15. Residua in the fulfillment of Eq. (1) without right-hand side for the eigenvectors associated to the 10 largest eigenvalues of the spectra from Fig. 14: (a) $n_s = 0$ and (b) $n_s = 5$.

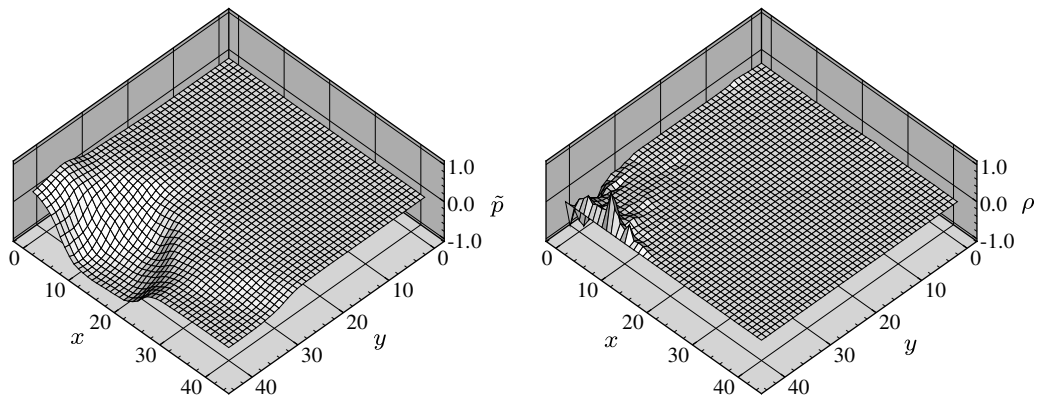


Fig. 16. Eigenvector (left) and corresponding residuum distribution (right) for the largest eigenvalue of the spectrum from Fig. 14(a) for the procedure with $n_s = 5$. Eigenvector and residuum are independently rescaled.

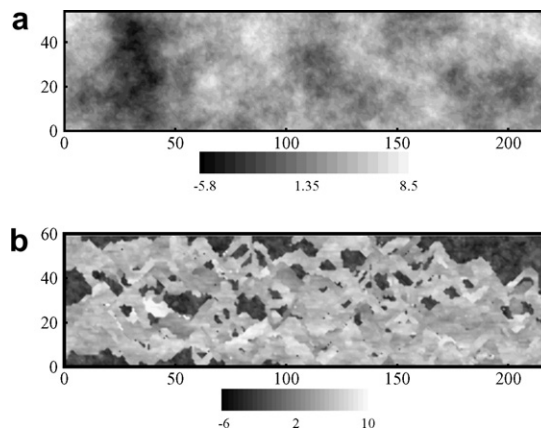


Fig. 17. Natural logarithm of k in the top (a) and the bottom (b) layers of the three-dimensional SPE10 test case.

method with slightly modified correction functions is employed and both basis and correction functions need to be updated in regions only where the total mobility changes are significant [22,23]. The computational cost of this algorithm is comparable with the one of the original MSFV method. But typically, as shown next, the accuracy of the solutions is dramatically improved.

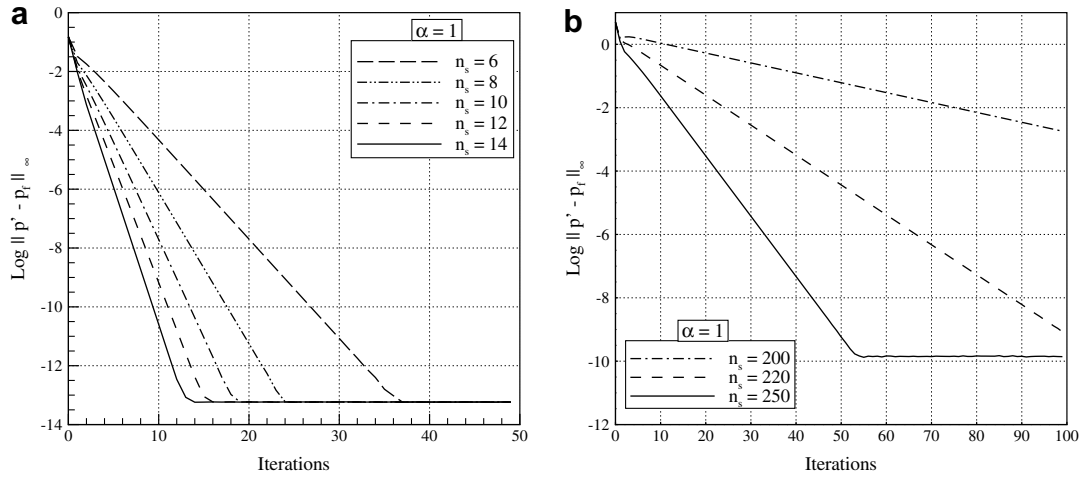


Fig. 18. Numerical convergence histories with the permeability field of [a] Fig. 17(a) and [b] Fig. 17(b) for $\alpha = 1$, $\Gamma = 11 \times 11$, and a fine grid of 220×55 .

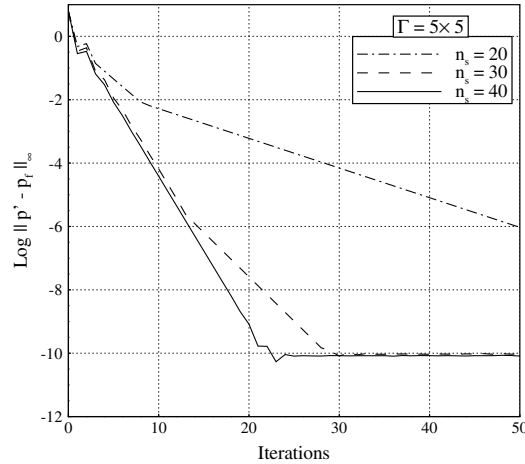


Fig. 19. Numerical convergence histories with the permeability field of Fig. 17(b) with a fine grid of 220×60 and $\Gamma = 5 \times 5$.

The i-MSFV method with infrequently updating the localization conditions is tested for two two-phase flow scenarios with a viscosity ratio μ_2/μ_1 of 10 and the relative permeabilities $k_{r1,2} = S_{1,2}^2$ ($S_{1,2} \in [0,1]$ are the phase saturations) for the first test case and $k_{r1,2} = S_{1,2}$ for the second one. The permeability fields of Figs. 17(a) and 20(a) are employed and the rectangular domains are discretized by 220×55 and 55×55 fine grids, respectively. In both cases, coarse grids consisting of volumes containing 11×11 fine cells with an aspect ratio of 10 are used and no-flow conditions are applied at the whole domain boundary. Initially, the domains are occupied with phase two and the less viscous phase is injected into the fine cell (1, 1). In the first scenario, production occurs from cell (220, 55) and in the second scenario from cell (55, 55). For the numerical solution of the phase transport equation, an explicit scheme was employed. Figs. 21 and 22 show the saturation maps for the two test cases after 0.165 pore volume injected (PVI). One can observe that the i-MSFV method with updating the correction function boundary conditions every 10th time step leads to results, which are virtually identical with the fine-scale reference solutions. On the other hand, the MSFV solutions of these challenging test cases show significant deviations from the reference.

7. Conclusions

In this paper, an iterative multiscale finite-volume (i-MSFV) method is devised. Each iteration, the MSFV fine-scale pressure solution is improved by a number of smoothing steps. The new approximation is then used to obtain better local boundary conditions for the new correction functions, which are required for the right-hand side of the coarse system. It is demonstrated for a wide range of difficult test cases that the i-MSFV method combined with a simple line-relaxation (LR)

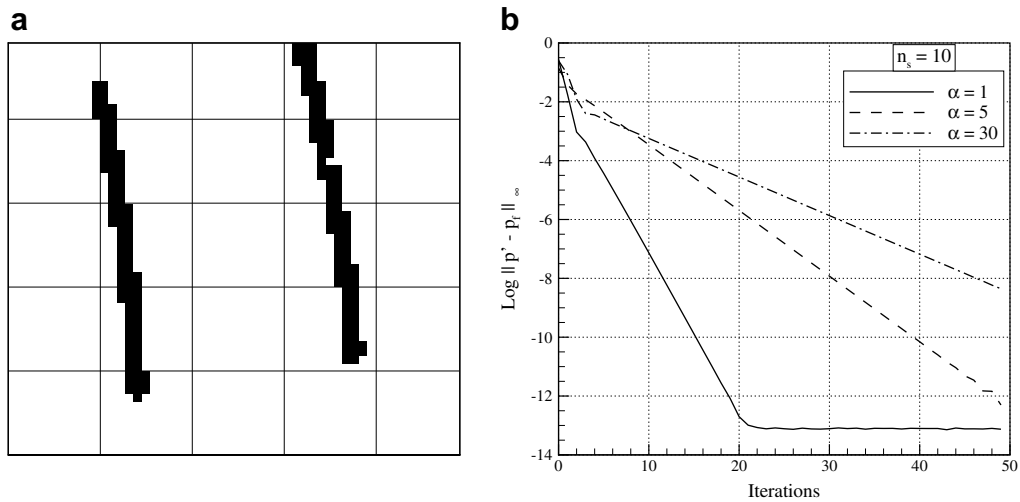


Fig. 20. (a) Shale layer test case together with 5×5 coarse grid. Each coarse cell contains 11×11 fine cells (not shown). The mobility in the domain is 10^{10} times higher than in the shale layers. (b) Numerical convergence history of the test case for $n_s = 10$ and different α .

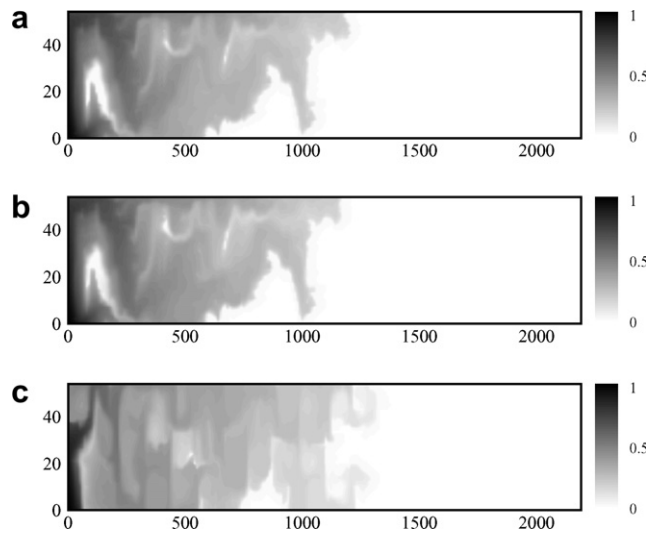


Fig. 21. Two-phase flow saturation maps for the SPE10 top layer test case with $\mu_2/\mu_1 = 10$, $k_{r1,2} = S_{1,2}^2$, and $\alpha = 10$ after 0.165 PVI: (a) fine scale, (b) i-MSFV method with local boundary conditions updated every 10th time step by applying 1 iteration and (c) standard MSFV method.

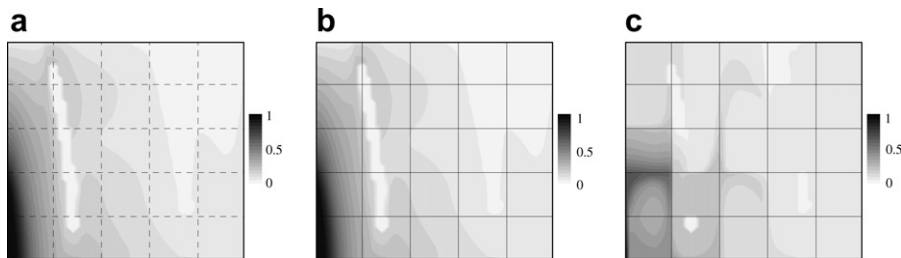


Fig. 22. Two-phase flow saturation maps for the shale layer test case with $\mu_2/\mu_1 = 10$, $k_{r1,2} = S_{1,2}$, and $\alpha = 10$ after 0.165 PVI: (a) fine scale result, (b) i-MSFV method with local boundary conditions updated every 10th time step by applying 1 iteration and (c) standard MSFV method.

smoother works well. Each LR step, an independent tri-diagonal system has to be solved for each grid line, e.g. with the Thomas algorithm which scales linearly with the problem size. Moreover, as shown earlier, LR is insensitive to the grid aspect ratio and the level of anisotropy, which is the reason that the i-MSFV method is very efficient for highly anisotropic prob-

lems. The number of iterations required by the overall solution algorithm is problem size independent, but more i-MSFV iterations are required as the coarse-grid-cell aspect ratio increases. However, the number of iterations reaches an asymptotic value beyond an aspect ratio of approximately 20. A further favorable property of the i-MSFV algorithm is that it can be operated anywhere between a multiscale method (without iterating it becomes identical to the MSFV method with correction functions) and an efficient linear solver. For example, if the iteration procedure is terminated before full convergence has been achieved, the method still delivers a conservative fine-scale velocity field. This is of relevance, e.g. if transport is solved on the fine grid. It is also shown that the i-MSFV method can be interpreted as a multigrid method which allows for extreme coarsening factors. An important property here is that no explicit upscaling is required.

Convergence studies with test cases involving shale layers, high coarse-cell aspect ratios, and layered permeability fields with sharp contrasts demonstrate the robustness and efficiency of the new method. Another important result is related to multiphase flow, where the mobility experiences changes due to evolving phase saturations. For the examples considered in Section 6.2 the i-MSFV method with one iteration every 10th time step leads to accurate solutions, that are very close to the fine-scale solution. This indicates that the efficiency of the i-MSFV method is similar to that of the MSFV method for complex two-phase flow problems. On the other hand, the i-MSFV solutions are more accurate and problems with high coarse-cell aspect ratios, strong anisotropy, and shale layers are avoided. Finally, more investigations for a wider range of multiphase flow scenarios are necessary in order to find a more specific criterion for the growth of errors versus the frequency and amount of iterative improvements of the localization conditions.

Acknowledgment

This work was partly supported by Chevron ETC, San Ramon, CA, USA.

References

- [1] X.H. Wen, J.J. Gómez-Hernández, Upscaling hydraulic conductivities in heterogeneous media, *J. Hydrol.* 183 (1996) ix–xxxii.
- [2] P. Renard, G. de Marsily, Calculating effective permeability: a review, *Adv. Water Res.* 20 (1997) 253–278.
- [3] C.L. Farmer, Upscaling: a review, *Int. J. Numer. Methods Fluids* 40 (2002) 63–78.
- [4] L.J. Durlofsky, Numerical calculation of equivalent grid block permeability tensors for heterogeneous media, *Water Resour. Res.* 27 (1991) 699–708.
- [5] Y. Gautier, M.J. Blunt, M.A. Christie, Nested gridding and streamline-based simulation for fast reservoir performance prediction, *Comput. Geosci.* 3 (3–4) (1999) 295–320.
- [6] T.Y. Hou, X.-H. Wu, A multiscale finite element method for elliptic problems in composite materials and porous media, *J. Comput. Phys.* 134 (1997) 169–189.
- [7] Z. Chen, T.Y. Hou, A mixed multiscale finite element method for elliptic problems with oscillating coefficients, *Math. Comput.* 72 (242) (2002) 541–576.
- [8] J.E. Aarnes, V. Kippe, K.-A. Lie, Mixed multiscale finite elements and streamline methods for reservoir simulation of large geomodels, *Adv. Water Resour.* 28 (3) (2005) 257–271.
- [9] J.E. Aarnes, On the use of a mixed multiscale finite element method for greater flexibility and increased speed or improved accuracy in reservoir simulation, *Multiscale Model. Simul.* 2 (3) (2004) 421–439.
- [10] P. Jenny, S.H. Lee, H.A. Tchelepi, Multi-scale finite-volume method for elliptic problems in subsurface flow simulation, *J. Comput. Phys.* 187 (2003) 47–67.
- [11] V. Ginting, Analysis of two-scale finite volume element method for elliptic problem, *J. Numer. Math.* 12 (2004) 119–141.
- [12] T.Y. Hou, X.-H. Wu, Z. Cai, Convergence of a multiscale finite element method for elliptic problems with rapidly oscillating coefficients, *Math. Comput.* 68 (227) (1999) 913–993.
- [13] P. Ming, X. Yue, Numerical methods for multiscale elliptic problems, *J. Comput. Phys.* 214 (2006) 421–445.
- [14] Y. Efendiev, T. Hou, X. Wu, Convergence of a nonconforming multiscale finite element method, *SIAM J. Numer. Anal.* 37 (2000) 888–910.
- [15] V. Kippe, J.E. Aarnes, K.-A. Lie, A comparison of multiscale methods for elliptic problems in porous media flow, *Comput. Geosci.*, in press, doi:10.1007/s10596-007-9074-6 (Special Issue on Multiscale Methods for Flow and Transport in Heterogeneous Porous media).
- [16] M.A. Hesse, B.T. Mallison, H.A. Tchelepi, Compact multiscale finite volume method for heterogeneous anisotropic elliptic equations, *SIAM Multiscale Model. Simul.*, (2008), in press.
- [17] I. Lunati, P. Jenny, Multi-scale finite-volume method for highly heterogeneous porous media with shale layers, in: *Proceedings of the 9th European Conference on the Mathematics of Oil Recovery (ECMOR)*, Cannes, France, 2004.
- [18] Y. Efendiev, V. Ginting, T. Hou, R. Ewing, Accurate multiscale finite element methods for two-phase flow simulations, *J. Comput. Phys.* 220 (2006) 155–174.
- [19] Y. Chen, L.J. Durlofsky, M. Geritsen, X.H. Wen, A coupled local-global upscaling approach for simulating flow in highly heterogeneous formations, *Water Resour. Res.* 26 (2003) 1041–1060.
- [20] Y. Chen, L.J. Durlofsky, Efficient incorporation of global effects in upscaled models of two-phase flow and transport in heterogeneous formations, *SIAM Multiscale Model. Simul.* 5 (2006) 445–475.
- [21] L.J. Durlofsky, Y. Efendiev, V. Ginting, An adaptive local-global multiscale finite volume element method for two-phase flow, *Adv. Water Resour.* 30 (2007) 576–588.
- [22] P. Jenny, S.H. Lee, H.A. Tchelepi, Adaptive multiscale finite volume method for multi-phase flow and transport, *SIAM Multiscale Model. Simul.* 3 (1) (2005) 50–64.
- [23] P. Jenny, S.H. Lee, H.A. Tchelepi, Adaptive fully implicit multi-scale finite-volume method for multi-phase flow and transport in heterogeneous porous media, *J. Comput. Phys.* 217 (2006) 627–641.
- [24] B. Rembold, P. Jenny, A multiblock joint pdf finite-volume hybrid algorithm for the computation of turbulent flows in complex geometries, *J. Comput. Phys.* 220 (1) (2006) 59–87.
- [25] H.A. Tchelepi, P. Jenny, S.H. Lee, C. Wolfsteiner, An adaptive multiphase multiscale finite volume simulator for heterogeneous reservoirs, SPE 93395, presented at the 19th SPE Reservoir Simulation Symposium, Woodlands, TX, USA, 2005.
- [26] I. Lunati, P. Jenny, Multiscale finite-volume method for compressible multiphase flow in porous media, *J. Comput. Phys.* 216 (2) (2006) 616–636.
- [27] S.H. Lee, C. Wolfsteiner, H.A. Tchelepi, Multiscale finite-volume formulation for multiphase flow in porous media: black oil formulation of compressible, three-phase flow with gravity, *Comput. Geosci.*, 2008, available online.
- [28] H. Zhou, H.A. Tchelepi, Operator based multiscale method for compressible flow, SPE 106254, presented at the SPE Reservoir Simulation Symposium, Houston, TX, USA, 2007.

- [29] I. Lunati, P. Jenny, Multiscale finite-volume method for density-driven flow in porous media, *Comput. Geosci.*, 2008, available online.
- [30] I. Lunati, P. Jenny, A multiscale finite-volume method for three-phase flow influenced by gravity, in: *Proceedings of XVI International Conference on Computational Methods in Water Resources (CMWR XVI)*, Copenhagen, Denmark, 2006.
- [31] I. Lunati, Multi-scale finite-volume method for multiphase flow with gravity, Technical report, Chevron/Schlumberger Alliance Technology, 2006.
- [32] I. Lunati, P. Jenny, An efficient multiscale finite-volume method for modeling density driven flow in porous media, *Geophys. Res. Abst.* 9 (06337) (2007).
- [33] C. Wolfsteiner, S.H. Lee, H.A. Tchelepi, Well modeling in the multiscale finite volume method for subsurface flow simulation, *SIAM Multiscale Model. Simul.* 5 (3) (2006) 900–917.
- [34] P. Jenny, Well modeling in the multi-scale finite volume context based on correction functions, in: *6th International Congress on Industrial and Applied Mathematics (ICIAM 07)*, GAMM section, Zurich, Switzerland, 2007.
- [35] P. Jenny, I. Lunati, Treatment of complex well configurations with the multi-scale finite volume method, (2008), submitted for publication.
- [36] M.A. Christie, M.J. Blunt, Tenth spe comparative solution project: A comparison of upscaling techniques, SPE 66599, presented at the SPE Symposium on Reservoir Simulation, Houston, February, 2001.
- [37] P. Jenny, I. Lunati, Treating highly anisotropic subsurface flow with the multiscale finite-volume method, *SIAM Multiscale Model. Simul.* 6 (1) (2007) 308–318.
- [38] U. Trottenberg, C.W. Oosterlee, A. Schuller, *Multigrid*, Elsevier Academic Press, 2001.
- [39] D. Peaceman, H. Rachford, The numerical solution of elliptic and parabolic differential equations, *J. SIAM* 3 (1955) 28–41.
- [40] K. Aziz, A. Settari, *Petroleum Reservoir Simulation*, 2nd ed., Blitzprint Ltd., 2002.
- [41] Y. Chen, B.T. Mallison, L.J. Durlofsky, Nonlinear two-point flux approximation for modeling full-tensor effects in subsurface flow simulations, *Comput. Geosci.*, 2008, available online.